Original article

The absorption effect and mechanism of graphene oxide removal from aqueous solution by basalt stone power

Ping Jiang, Fuping Wang, Wei Wang, Na Li [*], Shimeng Yu

Shaoxing Key Laboratory pf Interaction between Soft Soil Foundation and Building Structure, School of Civil Engineering, Shaoxing University, Shaoxing 312000, China

ABSTRACT

Graphene oxide (GO) is a novel carbon material utilized extensively for diverse industrial applications. When exposed to environmental elements like sunlight and chlorination, GO can undergo a series of physical and chemical transformations, and its presence in water and the environment can endanger ecosystems. Therefore there is a need for methods that can effectively remove GO from water. Accordingly, we delve into the efficacy of basalt stone powder (BSP) as an adsorption medium for purifying aqueous solutions of GO. We examine the impact of various experimental parameters—namely pH, initial solution concentration, adsorbent mass, contact duration, and ambient temperature—on GO adsorption, employing the method of controlled variables. The adsorption efficacy is notably influenced by the pH level. At an acidic pH of 3, an initial GO concentration of 80 mg/L, an adsorbent dosage of 50 mg, and a temperature of 303 K (approximately 30 °C), the adsorption removal efficiency reaches an impressive 99 %, boasting a maximum adsorption capacity of 112 mg/g. Dynamically, the adsorption kinetics align most closely with a pseudo-first-order model, achieving equilibrium after 24 h. Thermodynamic analyses reveal that the Langmuir isotherm model most accurately describes the adsorption behavior, indicating an enhancement in BSP's adsorption capacity for GO as temperature rises. Based on thermodynamic equations, the adsorption of GO onto BSP is deduced to be a spontaneous process. Our findings illustrate BSP's considerable potential in the treatment and removal of GO from water, and therefore it may prove useful in environmental remediation efforts.

1. Introduction

Graphene oxide (GO) features a variety of functional groups on its surface, such as carboxyl (–COOH), hydroxyl (–OH), and ketone (−C = O) groups (see Fig. 1) (Rout and Jena, 2022), causing GO to have weak ionic dipole interactions, and leading to its strong repulsion of anions. Moreover, as a derivative of graphene, GO possesses exceptional strength and toughness, is used to enhance the performance of polymers like cement soil and ceramics, and holds great potential in various scientific fields. However, the oxygen-containing groups in GO's molecular structure cause it to aggregate in aqueous solutions (Rout and Jena, 2021), and traditional centrifugation or filtration methods struggle to remove GO from such solutions (Anuma et al., 2021). Separating GO during water treatment is challenging and may lead to secondary pollution (Chowdhury and Balasubramanian, 2014). Some studies have demonstrated that once released into the environment, GO can induce biotoxicity (Zhao et al., 2021; Bytešníková et al., 2023). For instance

bacterial cells exposed to GO developed toxicity through mechanisms such as deposition and direct contact with sharp nanosheets that cause membrane stress (Seabra et al., 2014), with higher concentrations leading to greater toxicity. The inherent toxicity of GO limits its widespread application, and thus there is a desire to mitigate GO's environmental impact.

To address the issue of GO environmental pollution, various methods have been employed to reduce its impact, such as filtration (Semghouni et al., 2020), biotreatment (Kalsoom and Batool, 2020), chemical precipitation (An et al., 2023), oxidation (Bandara et al., 2020), photocatalytic degradation (Samuel et al., 2023), and adsorption (Xiang et al., 2021). Among these, adsorption stands out for its flexibility, cost-effectiveness, ease of operation, and high removal efficiency, making it one of the most promising techniques (Rout and Jena, 2023). Studies have shown that upon entering the environment, GO interacts and reacts with surface minerals (Chen et al., 2021); and solid mineral waste like iron tailings can effectively remove GO from aqueous solutions (Zhou

---

* Corresponding author.
E-mail addresses: jiangping@usx.edu.cn (P. Jiang), 22020859023@usx.edu.cn (F. Wang), wellswang@usx.edu.cn (W. Wang), lina@usx.edu.cn (N. Li), 21020859111@usx.edu.cn (S. Yu).
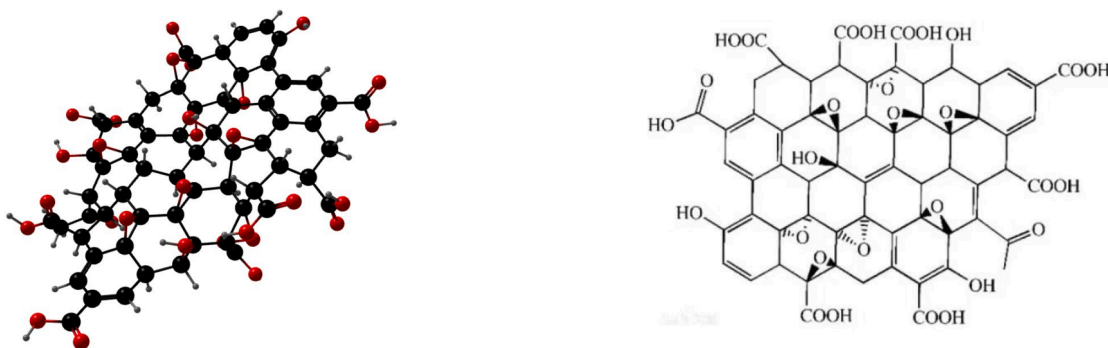
Fig. 1. The crystal structure and 3D model of oxidized graphene.

et al., 2021). At present, there is a noticeable lack of comprehensive research on adsorbent materials. The relatively large particle size of these adsorbents, coupled with their densely-packed pore space and limited surface area, significantly hampers their adsorption efficiency (Li et al., 2022). Additionally, some adsorbents may cause secondary pollution to the environment (Al-Bermany and Chen, 2021). Furthermore, the desorption performance of current adsorbents is limited. Desorption abilities of adsorbents are crucial as they directly affect renewability and recyclability, thereby impacting the economic and environmental sustainability of their use. An ideal adsorbent should be able to restore its original adsorption capacity through a simple desorption process, allowing repeated use. The cyclic use of adsorbents can reduce treatment costs and minimize the consumption of raw materials, thereby reducing the environmental footprint of such processes. In practical engineering applications, adsorbents often need to be reused multiple times instead of just once, and importantly, GO can be recovered given an effective desorption process.

Utilization of machine-made sand is increasing, and the sand-making process inevitably produces a large amount of Basalt stone powder (BSP), which leads to significant land resource use and poses safety risks. Therefore, enhancing the recovery rate of BSP is an urgent issue (Shen et al., 2022). In fact, many scholars have used BSP as an effective adsorbent to reduce environmental pollution. Studies have shown that BSP's unique porous structure and larger surface area, which contribute to more adsorptive sites, significantly enhance its adsorption efficiency. Additionally, BSP is a cost-effective and environmentally-friendly material, making it particularly relevant to sustainable environmental management. Researchers such as Almeida (Almeida et al., 2022) investigated the removal rates of dyes by basalt and granite stone powder, with adsorption rates reaching up to 92 %. Similarly, Pak et al. (Pak et al., 2021) synthesized composite microspheres from stone powder, chitosan, and magnetic hematite for adsorbing arsenic and lead from the environment. Furthermore, Alemu et al. (Alemu et al., 2019) investigated the adsorptive effect of BSP on chromium wastewater using a batch adsorption method, with the results showing that foamed basalt has good potential for treating wastewater containing chromium. Given that the standard size of stone powder is less than or equal to 0.075 mm, its smaller adsorbent particles offer a larger relative surface area and a greater number of adsorption sites (Matsuka et al., 2022), providing a faster adsorption rate. Thus, adsorbing GO with BSP to form flocs is an effective way to control the dispersion of GO's toxicity.

In this study, we utilize BSP as an adsorbent to effectively reduce GO pollution in the environment and increase the recovery rate of BSP. The adsorptive effects of BSP on GO are investigated by varying factors such as pH, adsorbent mass, initial solution concentration, temperature, and contact time. The adsorption mechanism was characterized by microscopic analysis of the crystal structure, molecular structure of functional groups, elemental types and valence states, morphological structure, and potential detection before and after adsorption. These experiments provide a foundation for the effective application of BSP adsorption of

Table 1
Main chemical composition of GO.

Main element	C	O	H	S
Content(%)	41.7	51.49	2.41	2

GO in future engineering projects.

2. Materials and methods

2.1. Materials

The GO used in our study was produced by the Suzhou Carbon Fountain Technology Company (Suzhou, China). The purity of the GO is greater than 99 % (by weight), and has a chemical formula of $C_6O_{11}(OH)_2$. Analysis of its elements is shown in Table 1. We used a LA-960 laser system to investigate the GO, with the results shown in Fig. 2 (a). As a control variable, 18.2 MΩ·cm ultrapure water from a UPW-R ultrapure water meter was used (LEICI, Shanghai, China). The BSP was a common mechanism sand BSP, and Table 2 shows its main chemical composition. The bulk density of the BSP was 2300–2800 kg/m^3, and it was produced in the Shaoxing Central Asia Industrial and Trade Park. The BSP was passed through a 0.075 mm sieve before use to ensure that it met the BSP particle size standard and normalize the impact of particle size on the experimental results. Laser particle size analysis was used to measure the BSP, with the results shown in Fig. 2 (b).

2.2. Test methods

2.2.1. Sorption experiment

The experimental procedure for the sorption experiments (desorption and adsorption) is as follows: 1) Add 2 mL of GO after ultra-sonication into 50 mL of ultrapure laboratory water; the initial concentration of GO was 80 mg/L. 2) The pH is balanced by the addition of 0.1 mol/L (0.3646 % by weight) HCl and 0.1 mol/L (0.4 % by weight) NaOH, and after that, weighed BSP is added as an adsorbent. 3) Next, the BSP is placed in a thermal oscillator at a thermostatic temperature of 303 K with an oscillation rate of 240 RPM (KS 4000 i, IKA, Germany) for 3 h to make full contact (Li et al., 2022; Li et al., 2022). 4) Finally, the sample is allowed to stand for 24 h in a dry and thermostatic environment (101-2BS, LICHEN, China). Afterwards, a pipette is used to transfer the upper clear liquid into a measuring cylinder, and pure laboratory-water is added dropwise until reaching 25 mL. Then the solution is analyzed using a UV–visible spectrophotometer (UV 75 N, Youke, Shanghai, China) at 210 nm to obtain the transmittance, and the residual GO content of the supernatant is derived using the standard curve. Since error is inevitable in this testing process, the spectrophotometric test was repeated three times and then averaged (Sakr et al., 2022); to ensure
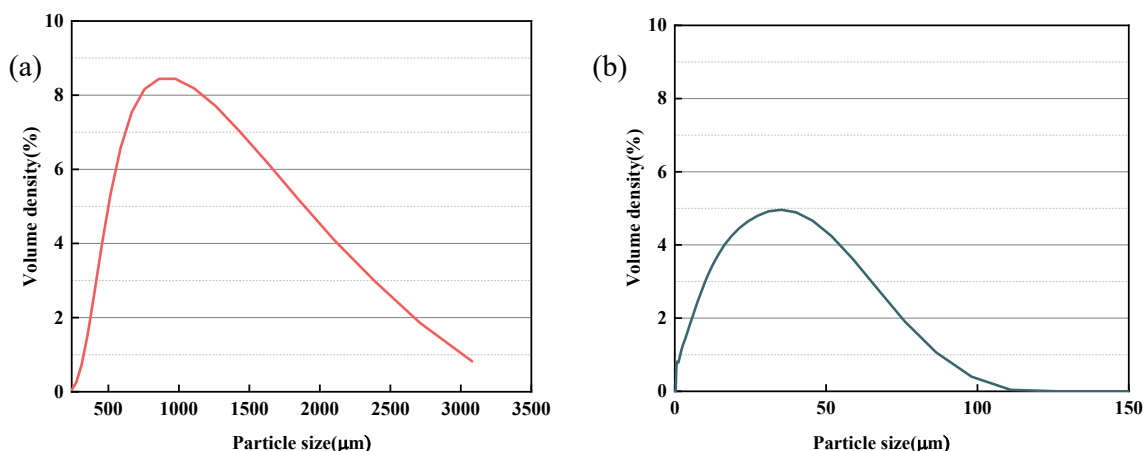
Fig. 2. Particle size distribution of GO(a) and BSP(b).

Table 2
Chemical composition table of BSP.

Chemical composition	SiO_2	Al_2O_3	CaO	MgO	Fe_2O_3	FeO	Na_2O	K_2O	P_2O_5	TiO_2	MnO	other
Content(%)	48.79	13.06	8.6	3.5	5.6	8.93	2.64	1.28	0.33	3.05	0.17	4.05

Table 3
Test mix ratio.

Mass of BSP	pH	Initial concentration of GO	Shaking Time	Quiescent Time	Temperature
mg		mg/L	h	h	K
50	3, 4, 5, 6, 7, 8, 9, 10	80	3	24	303
30, 40, 50, 60, 70, 80, 90, 100, 110	3	80	3	24	303
70	3	40, 60, 80, 100, 120	3	24	303
70	3	80	3	24	293, 303, 313
70	3	80	3	48	303

the relative standard deviation (RSD) was less than 5 %. The residual GO concentration in the supernatant was calculated from the standard curve. The sorption percentage R, sorption capacity Q_e(mg/L) and partition coefficient K(g/L) were calculated using Eqs. (1), (2), and (3) (Abdallah and Taha, 2012).

$$R = \frac{C_0 - C_e}{C_0} \quad (1)$$

$$Q_e = \frac{(C_0 - C_e) \times V}{m} \quad (2)$$

$$K = \frac{Q_e}{C_e} \quad (3)$$

Where C_0(mg/L) is the concentration of GO before adsorption, C_e(mg/L) is the concentration of GO in the supernatant after sorption, V(mL) is the volume of GO, m(mg) is the Quality of BSP and C_e(mg/L) is the sorption capacity.

As shown in the fit ratio in Table 3, because the pH of the GO, the adsorbent content, and the initial solution concentration have different degrees of influence on the sorption effects, the test was conducted with the control variable method in order to derive the optimal parameters. With an adsorbent mass of 50 mg at 303 K and a GO concentration of 80 mg/L, the solution with a pH range of 3–10 was obtained by titration using trace amount of HCl and NaOH. Subsequently, the mass of BSP gradually increased within the range of 30–110 mg, and then finally the GO solution concentration was varied in the range of 40–120 mg/L to obtain the optimum parameters for BSP.

The kinetic data for the sorption process were used in quasi-primary and quasi-secondary equations. The sorption process and thermodynamics of the sorption reaction were studied using the Freundlich and Langmuir models.

2.2.2. Material characterization

The crystal morphology of the materials was determined using X-ray diffraction (XRD Empyre, Malvern Corporation, UK) on a range of 5-90°. A Fourier Transform Infrared machine (FTIR IRPrestige-21, Shimadzu, TKY, Japan) was used to identify functional groups and chemical bonds in the wavenumber range of 500–4000 cm^{-1}, at room temperature. X-ray photoelectron spectroscopy (XPS ESCALAB 250XI) was used to analyze the elemental chemistry of the materials at AL-Kα X-ray source states. The size and shape of materials before and after sorption were recorded and observed by a scanning electron microscope (SEM JSM-6360 LV, JEOL, TKY, Japan) and a transmission electron microscope (TEM JEM 2100F, JEOL, TKY, Japan). The shape of the material surface and the height changes before and after the reaction were analyzed by an atomic force microscope (AFM Bruker Dimension lcon). The dispersion stability of the GO solution was measured using a nanopotential analyzer (Zeta, Nano-ZS 90, Malvern Corporation, UK).

2.2.3. Desorption experiment

The desorption test was conducted immediately after the adsorption test in the following steps: 1) After the adsorption test, the adsorbed precipitate was suctioned out and then centrifuged at 18,000 RPM for 2 min before being dried in a vacuum drying machine. 2) The dried samples were added to three different pH solutions (2, 7, and 10) for desorption (Liu et al., 2021). To ensure sufficient contact between the desorption agent and BSP/GO, they were stirred in a magnetic stirrer for 24 h. 3) The desorbed precipitate was suctioned out, vacuum dried again, and then subjected to adsorption testing to determine the
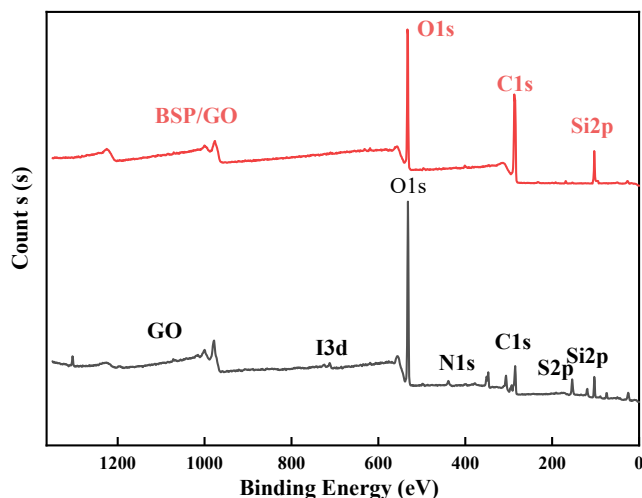
Fig. 3. XPS spectra of GO and BSP/GO.
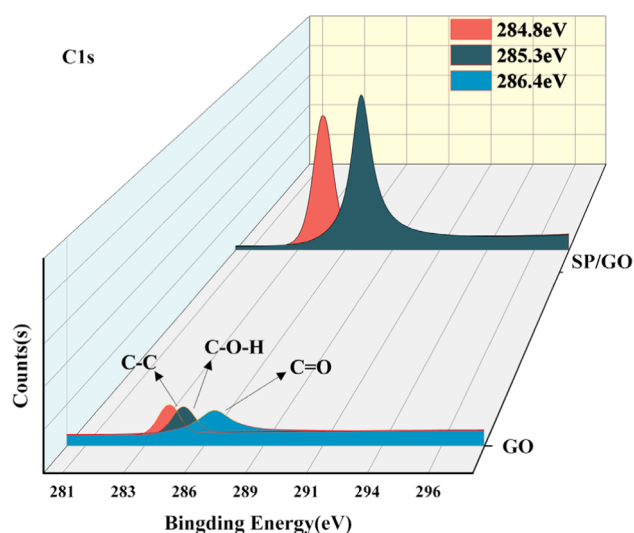
Fig. 4. Height deconvolution of C1s spectra.
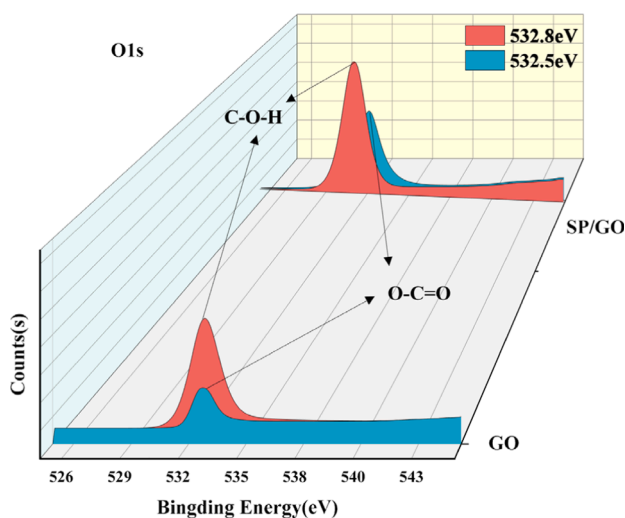
Fig. 5. Height deconvolution of O1s spectra.

desorption rate.

3. Results and discussion

3.1. Microtesting and materials characterization

3.1.1. XPS and AFM analysis

The spectra measured by the XPS are located at 532 eV, 284 eV, 184 eV, and 102 eV as shown in Fig. 3, corresponding to O1s, C1s, S2p, and Si2p, respectively. This confirms that the material mainly consists of O, C, S, and Si. The C1s height of GO has three peaks at 284.8 eV, 285.3 eV, and 286.4 eV, which are the C–C, C-O–H, and C = O of GO, respectively. As shown in Fig. 4 and Fig. 5, the height deconvolution of O1s spectra was carried out, and the O1s of GO were deconvolved into two peaks at 532.5 eV and 532.8 eV (Kumar and Masram, 2021). The intensity of the C1s peak with O1s was larger for SP/GO compared to GO, and the areas of the peaks were increased by 235 % and 32 %, indicating that GO aggregated on the BSP. An important parameter characterizing the degree of oxidation of GO is the fraction of carbon (Zhao et al., 2015), and characteristic peaks of C1s and O1s were observed in GO mainly at 298.08 eV and 544.97 eV. The O/C ratio of BSP/GO (1.09:1) is lower than the O/C ratio of GO (4.23:1), which is because the functional groups gradually reach saturation during the sorption process, reducing the degree of oxidation and gradually increasing the carbon fraction. Additionally, the characteristic peaks of Si2P were observed to be strengthened in the spectra of BSP/GO, and Si^{4+} was bonded during the sorption process, thus increasing the binding energy (Zhang et al., 2021).

The AFM images of GO and BSP/GO are shown in Fig. 6, to visualize the corresponding surface structure and material thickness. Comparing the AFM images of GO and BSP/GO, the surface of the BSP/GO is sharper and the range of the surface height (between 0 and 84 nm) is much higher than that of the GO surface (between 0 to 63 nm). Furthermore, the image of the BSP/GO no longer showcases the single-layer lamellae that GO displays. In addition, by measuring the maximum drop height, it was found that the maximum drop of 76.1 nm for BSP/GO was larger than the maximum drop of 43.36 nm for GO, indicating that when BSP adsorbs GO on the surface, the special particle shape of BSP is more prominent. Therefore, the BSP can effectively adsorb GO.

3.1.2. XRD and FTIR analysis

As shown in Fig. 7, an intense and broad diffraction peak (0 0 3) at 2θ = 10.8° was found in the XRD spectrum of GO, and the corresponding layer spacing was calculated as 0.88 nm according to Eq. (4), indicating a loosely-layered structure (Indujalekshmi et al., 2023), which is in agreement with the SEM image. In Eq. (4), n is the number of diffraction levels, λ (nm) is the X-ray wavelength, d (nm) is the layer spacing, and θ (°) is the diffraction angle. While two strong diffraction peaks appeared at 2θ = 26.6°(0 1 1) and 2θ = 29.4°(1 0 4) in the spectrum of the BSP, which were analyzed by the PDF card as indicators of quartz (SiO2), the diffraction peaks were still visible in the BSP/GO composite, confirming the sorption of GO on the surface of BSP. The height of the 011 absorption peaks after the sorption of GO by SP decreased from 12399 mV to 9432 mV, along with the height of the 104 diffraction peak from 10244 mV to 6804 mV. The disappearance of the 003 diffraction peak can be explained by GO undergoing surface-edge crosslinking with other materials, causing its corresponding characteristic peaks to become weaker or undetectable, again indicating that the BSP effectively adsorbs GO (Xu et al., 2008; Cai and Song, 2007).

$$n\lambda = 2d\sin\theta \tag{4}$$

Where n is the number of diffraction levels, λ (nm) is the X-ray wavelength, d (nm) is the layer spacing, θ (°) is the diffraction angle.

The molecular structure and chemical bonds of BSP and BSP/GO were determined using FTIR as shown in Fig. 8. The sorption peak appearing at 3450 cm^{-1} is the intermolecular stretching vibration of
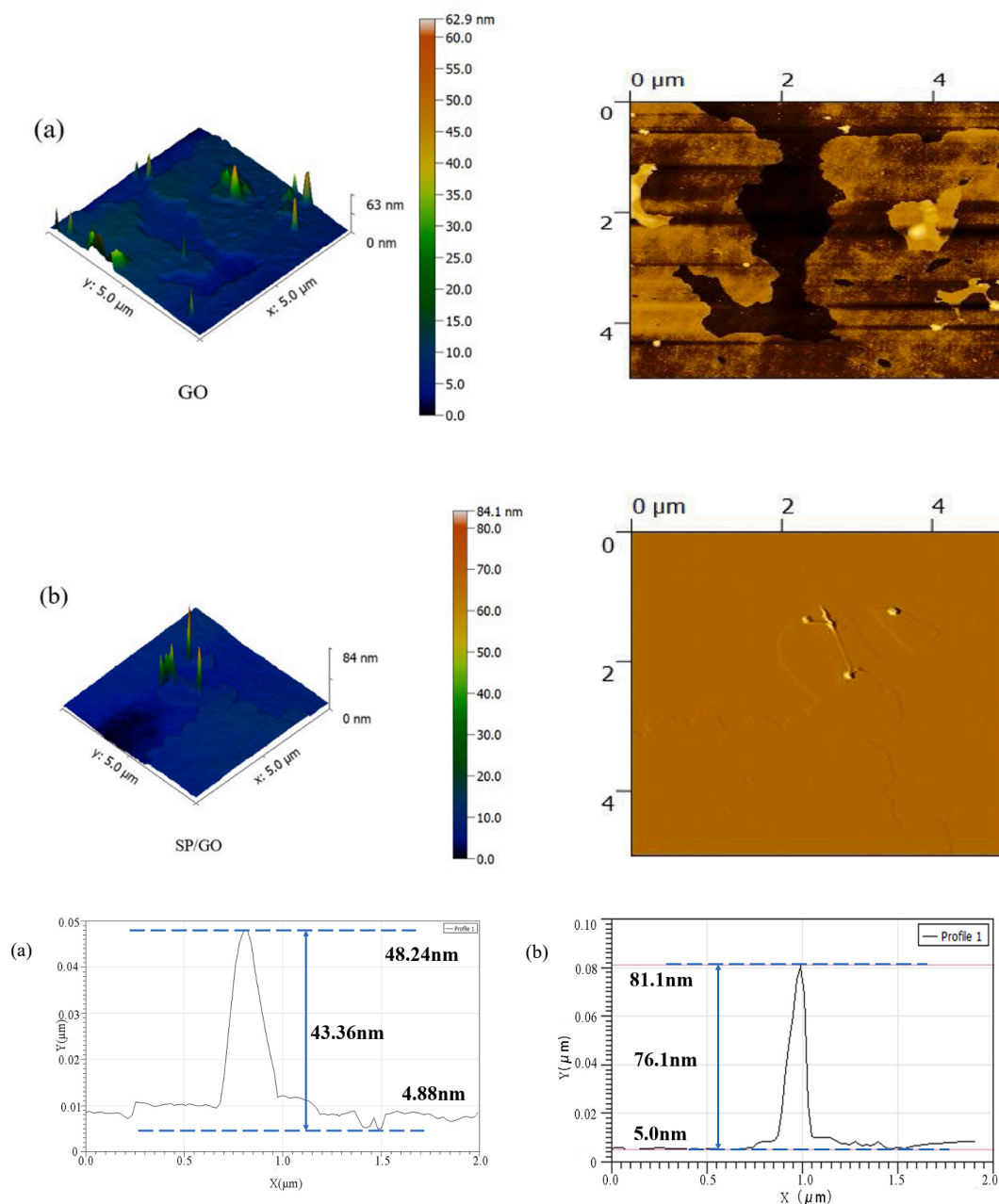
Fig. 6. AFM plots of GO and BSP/GO.

hydroxy-OH. In addition, the characteristic peaks at 1646 cm^{-1} and 1362 cm^{-1} correspond to the C $=$ O and C $=$ C vibrations of GO (Chen et al., 2011), respectively. The spectrum weakened at 1088 cm^{-1}, and new peaks were generated at 810 cm^{-1} and 792 cm^{-1}. The peak at 1088 cm^{-1} is related to the siloxane group (Zhang et al., 2018; Marcano et al., 2010; Zhang et al., 2014). The vibration band at 792 cm^{-1} corresponds to the Si-O-Si group. These data confirm the formation of SiO2/GO. After the adsorption of GO, an enhancement was observed at 792 cm^{-1} (Lin et al., 2021), corresponding to the asymmetric and symmetric stretching of the siloxane group in the BSP particles. A weaker peak was observed near 460 cm^{-1} due to the presence of U-O groups. Therefore, BSP exhibits excellent adsorption performance for GO.

3.1.3. SEM and TEM analysis

It can be seen from Fig. 9(b) that GO is a monolayer nanosheet with irregular edges. The SEM images show that GO has a smooth surface, less fragmentation of the lamellae, a high degree of folding on the surface,

and has an irregular structure with a corrugated shape. The TEM images showcase the GO's laminated structure as shown in Fig. 9(a), with a severe overlapping of the lamellae and uniformity of the lamellae surfaces. The folding and bending of the lamellae suggests that the rigidity of the graphene has been lost, indicating that GO has a larger number of covalent groups linked to its surface relative to graphene (Sysoev et al., 2023). From Fig. 9(d), it is clear that the BSP shows a granular structure with large pore space between the dispersed particles. From Fig. 9(c), the TEM image shows that the BSP is irregularly shaped. When the GO meets the BSP particles, it will adhere to the surface of the irregular BSP as shown in Fig. 9(f), which is the same result as the AFM test mentioned above. According to the laser particle size analysis, the GO has a large surface area of 5.86 m^2/g, and the surface area and particle size of GO particles should indeed be greater than that of BSP (Zhao et al., 2021). As shown in Fig. 9(e), BSP has accumulated a large amount of GO, which shows that the BSP has strong sorption properties for GO.
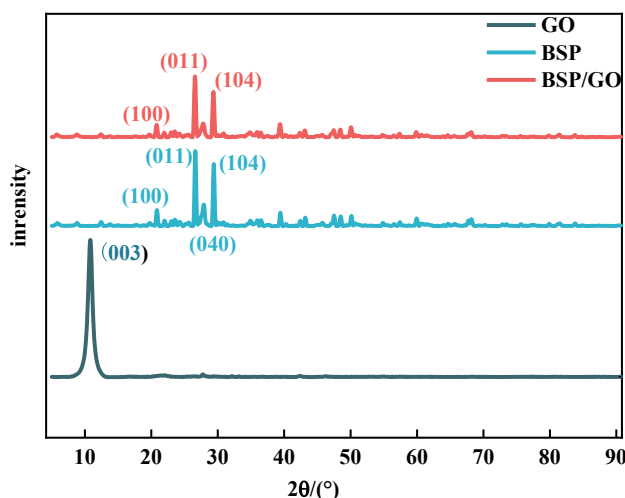
Fig. 7. XRD plots of GO and BSP/GO.
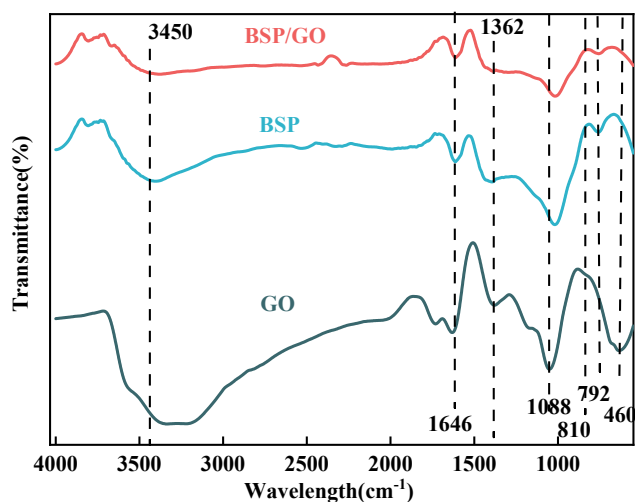
Fig. 8. FTIR spectra of GO and BSP/GO.

3.2. Sorption of GO by BSP

3.2.1. Effect of pH and zate potential analysis

The acidity and alkalinity of GO solutions significantly influence the sorption capacity of BSP. Fig. 10 illustrates the sorption behavior of BSP within a pH range of 3 to 10. Optimal sorption outcomes were observed at a pH of 3, including a maximum sorption rate of 95 %, a capacity of 76 mg/g, and a partition coefficient of 21. Electrostatic interactions, hydrogen bonding, and π-π interactions are identified as the principal mechanisms influencing sorption efficiency (Rout and Jena, 2021). With an increase in the GO solution's alkalinity, the electrostatic attraction between the cyclic aromatic structures of GO and the cations diminishes, leading to reduced sorption rates and capacities (Fan et al., 2017). Hence, an acidic pH of 3 is identified as the optimal condition for sorption. The abundance of functional groups such as hydroxyl, carboxyl, and carbonyl at the edges of the GO structure contributes to its interaction with water, releasing hydrogen ions and thus increasing the solution's acidity. The degree of GO oxidation is inversely correlated with the pH level, highlighting the importance of a highly-acidic environment for efficient BSP sorption. Consequently, BPS emerges as an effective adsorbent for GO, especially in acidic conditions.

The relationship between the pH and zeta potential of BSP/GO is depicted in Fig. 11. It is evident that the zeta potential of BSP/GO

decreases with increasing pH, indicating that a strong alkaline environment enhances the solution's stability. Specifically, the potential decreases to 17.79 mV at a pH of 9, suggesting a significant reduction in the degree of protonation of functional groups (Anuma et al., 2021). These experimental findings align with the earlier pH testing results. Due to the abundance of oxygen-containing functional groups on GO's surface, and its isoelectric potential (IEP) ranging from 3 to 4, GO carries a negative charge at a pH of 7 (Chowdhury and Balasubramanian, 2014). This negative charge surrounding GO facilitates sorption via electrostatic interactions. The mineral composition of BSP includes Ca^{2+}, and previous studies have shown that Ca^{2+} can migrate across the bilayer and bond with oxygen-containing functional groups (Jiang et al., 2022). Consequently, electrostatic forces are generated, enhancing sorption capacity between the protonated adsorbent and adsorbate, leading to the formation of sorption salts (Lim et al., 2021). Therefore, the presence of cations in BSP augments its sorption capacity (Ando et al., 2010).

3.2.2. Effects of adsorbents

An important factor affecting the sorption of GO by BSP is the quality of the adsorbent, and many studies have shown that an increase in adsorbent mass within a certain range has a positive effect on sorption capacity and efficiency; however this increase in sorption capacity is limited to a certain range. This is because as the mass of the adsorbent increases, the comparative surface available for sorption also increases, and although this can provide more sorption sites, it also leads to competition between sorption sites and limitations on the mass transfer. As shown in Fig. 12, the sorption percentage increases rapidly as the mass of BSP increases from 30 mg to 110 mg, and for a GO solution volume of 50 mL, the optimum adsorbent mass is 70 mg, the sorption rate R is 91 %, the sorption capacity Q_e is 51.9 mg/g, and the partition coefficient K_d is 14. The sorption rate and sorption capacity decreased when the adsorbent mass continued to increase beyond 70 mg, because going beyond the optimum mass provided too many active sorption sites, and the GO in solution was further adsorbed. However the space for sorption on the surface of the BSP adsorbent had still not reached saturation.

3.2.3. The impact of GO concentration

Testing of BSP in aqueous GO solutions with different concentrations, from 40 mg/L to 120 mg/L sequentially, is shown in Fig. 13. As the GO concentration (and thus potency) rises, the indices began to increase under the driving force of the chemical potential gradient (Fan et al., 2017). When the sorption rate and distribution coefficient reached their maxima, the potency of GO was 80 mg/L, the sorption rate R reached 99 %, K_d was 433, and the sorption capacity Q_e was 112 mg/g. When the solubility continued to increase, the available space for sorption on the adsorbent surface was close to saturation, leading to decreases in the K_d and sorption rate. And because the chemical potential gradient continued to increase with higher GO concentration, the sorption capacity Q_e continued to increase and reached 167 mg/g at 120 mg/L.

3.2.4. Sorption kinetics of GO

The impact of contact time on the sorption effect is crucial, and thus we performed sorption kinetics experiments to investigate this relationship. We used the following formulas to fit the quasi-first order kinetics and quasi-second order kinetics (Vareda, 2023; Hassanin et al., 2022).

$$In(q_e - q_t) = Inq_e - K_1 t \tag{5}$$

$$tk_2 q_e = q_t + t K_2 q_e q_t \tag{6}$$

Here q_t represents the adsorption amount (mg/g) at time t, and K_1 and K_2 are the pseudo-first-order and pseudo-second-order adsorption rate constants (g/(mg·min)), respectively.

The effect of contact time between BSP and GO on sorption kinetics is
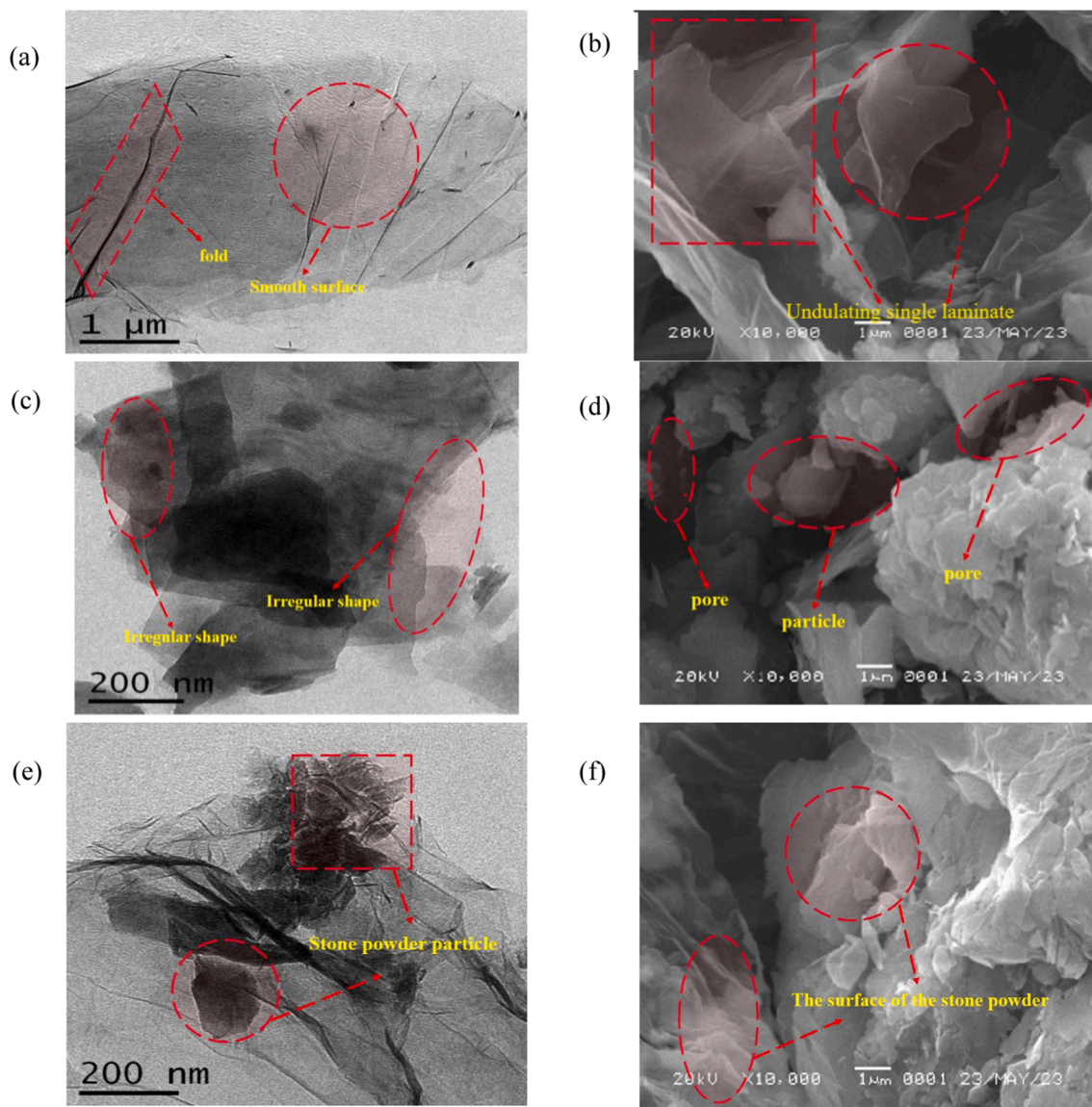
Fig. 9. TEM (a) and SEM (b) of GO, TEM (c) and SEM (d) of BSP, TEM (e) and SEM (f) of BSP/GO.
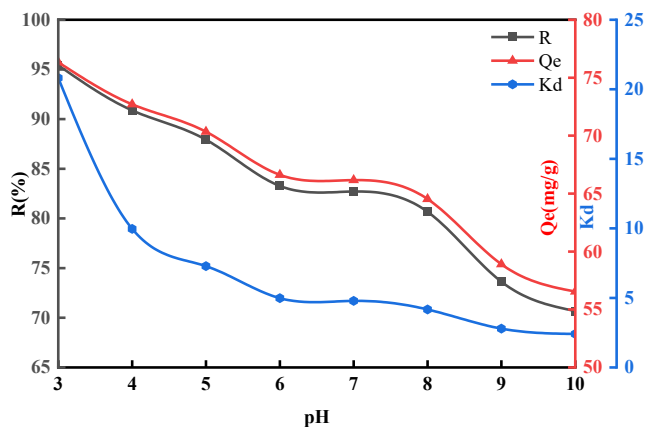
Fig. 10. The Effect of Different pH on the Sorption Ability of BSP.
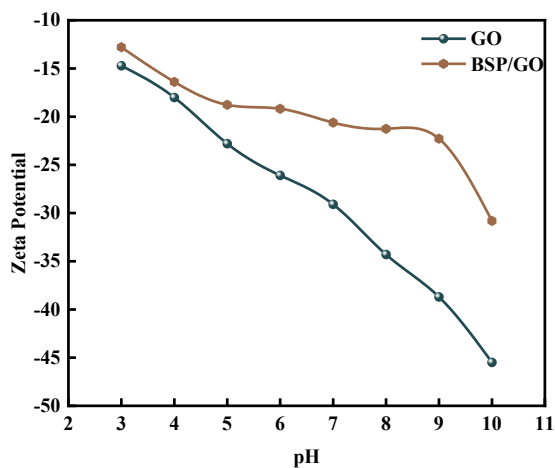
Fig. 11. GO and BSP/GO zeta potential diagram.

shown in Fig. 14. The sorption of GO rapidly increased to 54 mg/g within 500 min, because the surface of BSP has abundant adsorption sites (Gomaa et al., 2021), and the removal rate of GO was 91.7 %. As the

sorption reactions develop, the growth rate of the sorption rate
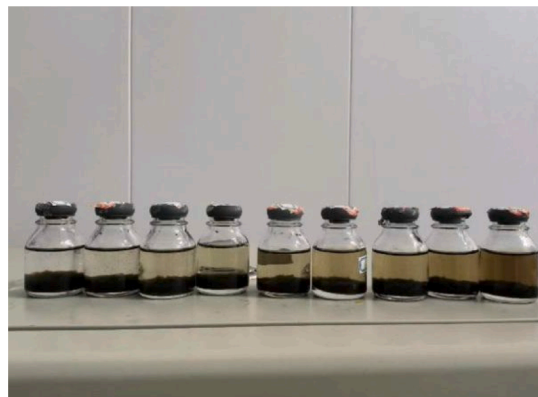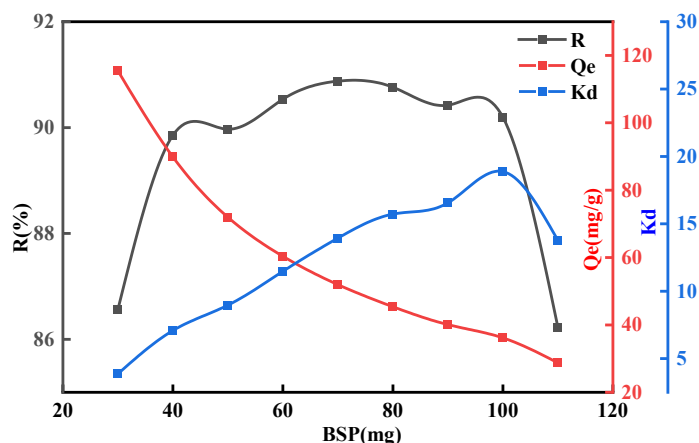
Fig. 12. Effect of adsorbent quality on the sorption capacity of BSP.
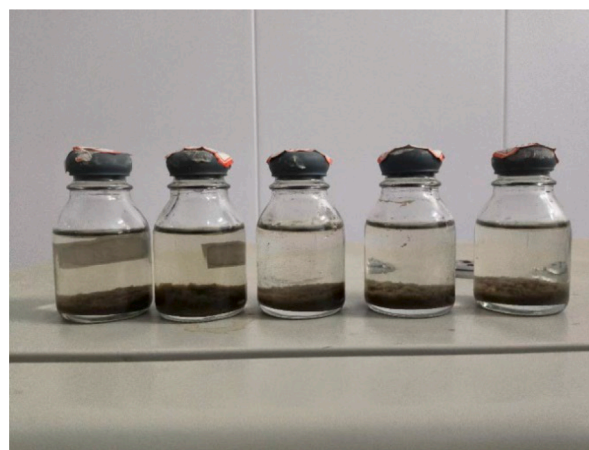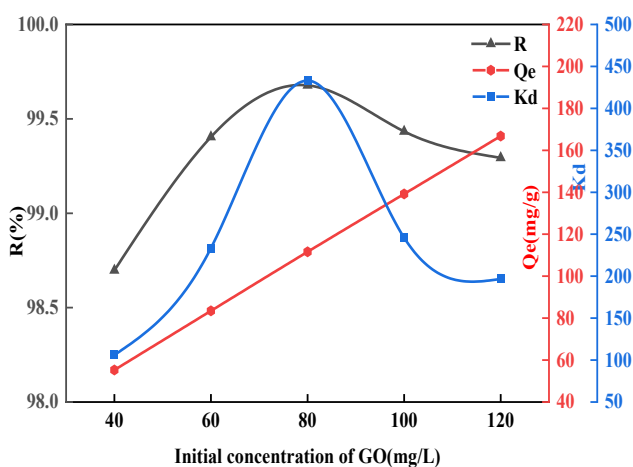
Fig. 13. Effect of initial concentration on GO sorption.
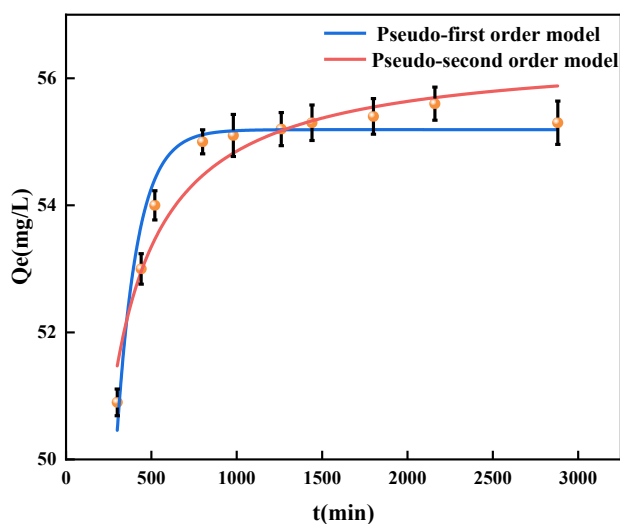
Fig. 14. Fitting curves of quasi-first order kinetics and quasi-second order kinetics.

gradually slows. Upon reaching equilibrium, the removal rate of GO is 98.8 %. The chemical composition of BSP leads to this sorption behavior for the following reasons (Chupakhin et al., 2009). First, the BSP contains 48.79 % SiO$_2$, a substance which has hydrophilicity. Additionally,

the surface of the BSP is very rough, with numerous protrusions and pits. The outer surface and pore outer surface of BSP are thus ideal locales for chemical activities that quickly cause binding to GO. With the passage of time, there is a reduction of space available for adsorption, and the concentration of GO in the solution decreases. Thus the driving force of the sorption of GO by the BSP decreases, and the polymers of GO go back into the solution. As a result, the sorption capacity remained stable after 1440 min (24 h).

From Table 4, we can see that the pseudo-first order kinetics model has a higher R^2 value compared to the pseudo-second order model. In addition, its calculated equilibrium sorption capacity q$_{cal}$ is more in line with the experimental values Q$_{exp}$. This indicates that the GO sorption process by BSP is more effectively described using quasi-first order kinetics, and the sorption process does not involve complex intermediates. Therefore, the adsorption of GO onto BSP is likely controlled by a chemical adsorption process (Yaroshenko et al., 2018; Allam et al., 2022; Cheira, 2020).

3.3. Sorption isotherms and sorption thermodynamics

The influence of environmental temperature on the sorption of GO by BSP was analyzed and predicted using a fitted isotherm model. Considering the ideal fitting as well as the nature of the experimental data, the temperatures of 303 K, 313 K, and 323 K are used as the data points in this study, and the classical thermodynamic models, Langmuir and Freundlich, are used to see which best fits the data.

The Langmuir isotherm equation assumes that the sorption sites are

Table 4

Parameters of quasi-primary and quasi-secondary dynamics.

C_O(mg/g)	Q_{exp}(mg/g)	Pseudo-first order model			Pseudo-second order model		
		K_1	q_{cal}(mg/g)	R^2	K_2	q_{cal}(mg/g)	R^2
80	53.93	0.008	55.19	0.95	0.00006	56.44	0.92
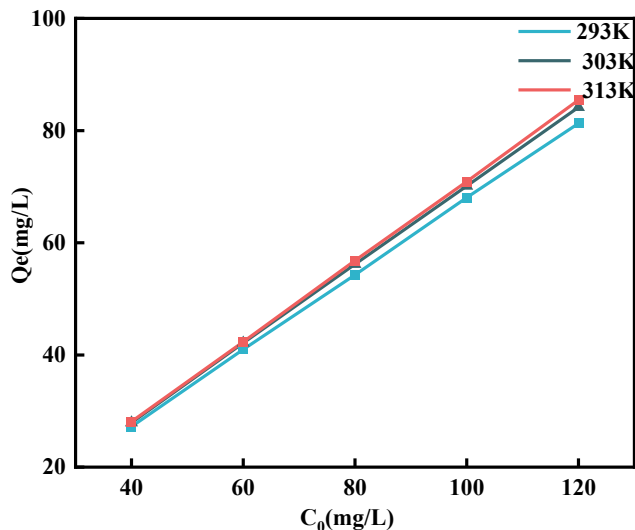
Fig. 15. Sorption isotherms.

uniformly distributed over the entire surface (Mollaamin and Monajjemi, 2023) and that there is only one adsorbate molecule at each sorption site. As a result; the Langmuir model is commonly used to evaluate molecular sorption in dilute solutions that come into direct contact with the surface. Its formula is shown in Eq. (7) (Eissa et al., 2023):

$$\frac{1}{Q_e} = \frac{1}{Q_m} + \frac{1}{K_L \times Q_m} \times \frac{1}{C_e} \tag{7}$$

The Freundlich isotherm equations are empirical equations that mainly describe the multilayer sorption process on non-uniform surfaces (Fouad, 2023). The formula we use is expressed in Eq. (8):

$$InQ_e = InK_F + \frac{1}{n} \times InC_e \tag{8}$$

Here, Q_e represents the equilibrium adsorption capacity (mg/g), C_e represents the equilibrium concentration (mg/L), Q_m represents the maximum adsorption capacity (mg/g), K_L represents the Langmuir adsorption equilibrium constant (L/mg), K_F represents the Freundlich adsorption equilibrium constant (L/mg), and n is a dimensionless constant related to the temperature and the adsorbent.

Temperature was used as a variable. The sorption isotherm was obtained as shown in Fig. 15. As the temperature increases, the sorption capacity becomes stronger, and the maximum sorption amounts Q_{max} are 81.28 mg/L, 84.16 mg/L, and 85.44 mg/L at 293 K, 303 K, and 313 K, respectively. The increase in sorption amount may be due to the fact that the momentum of the adsorbent in the solution increased as the temperature rose, which in turn increased the degree of contact and the

sorption capacity. However, the increase in temperature had less effect on the maximum sorption capacity, which only increased by 5.1 %. This shows that BSP is an excellent adsorbent for GO because of its stable sorption performance at normal temperatures (thus being practical for real world environments), and its resistance to temperature changes. Table 5 shows the parameters of the Langmuir and Freundlich
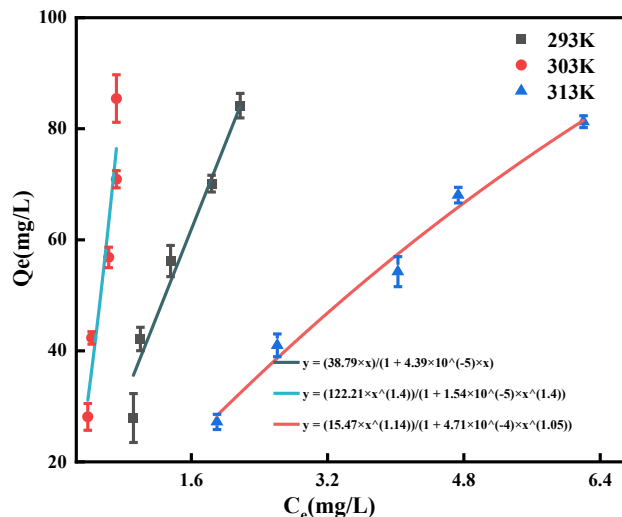
Fig. 16. Langmuir model fit curve.
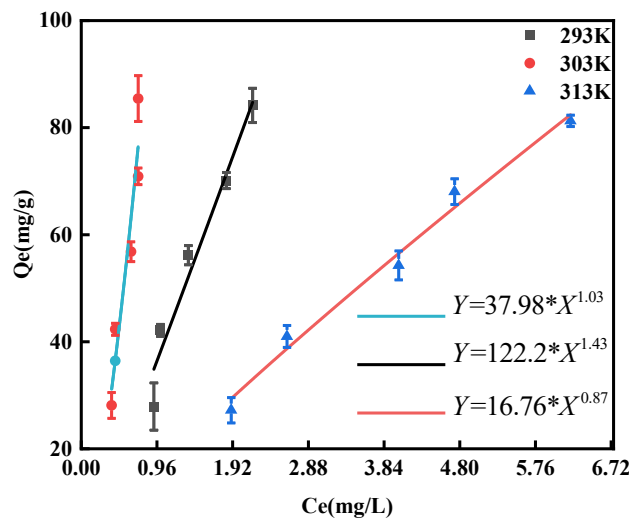
Fig. 17. Freundlich model fit curve.

Table 5

Parameters of Langmuir and Freundlich thermodynamic models.

C_O(mg/g)	pH	Temperature(K)	Langmuir			Freundlich		
			Q_{max}(mg/g)	K_L(L/mg)	R^2	K_F(L/mg)	1/n	R^2
80	3							
		293	881,532	0.00004	0.99	122.2	1.03	0.96
		303	7,914,215	0.00001	0.91	37.98	1.43	0.91
		313	237.46	0.07	0.99	16.76	0.87	0.99
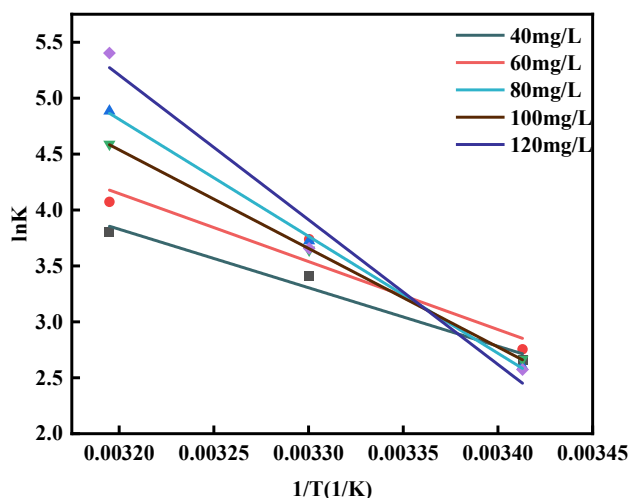
Fig. 18. Sorption thermodynamic fit.

Fig. 19. Desorption rate of BSP/GO for different pH values.

Table 6
Thermodynamic parameters.

C_0(mg/g)	ΔG			ΔH	ΔS
	293 K	303 K	313 K		
40	−9.25	−8.60	−6.93	865.98	387.43
60	−9.92	−9.42	−7.17	107.56	318.26
80	−11.90	−9.38	−6.77	73.31	272.28
100	−11.94	−9.17	−6.94	50.53	196.13
120	−13.16	−9.21	−6.70	43.49	171.02

equations, where K_L is the enthalpy of sorption, and K_F and $1/n$ are Freundlich isothermal constants; note that the larger K_F is, the larger the sorption of BSP on GO. When $1/n$ is close to zero, the sorption is non-homogeneous, and when $1/n$ is close to 1, the sorption process is chemisorption. On the other hand when $1/n$ is greater than 1, synergistic sorption occurs (Haghseresht and Lu, 1998). In Table 5; we can see that chemisorption occurs at 313 K, while synergistic sorption occurs at 293 K and 303 K. The sorption of GO by BSP was found to be very high at 293 K and 303 K. According to Table 3, the R^2 value of the Langmuir equation fitting result was higher than for the Freundlich, and the sorption of GO by BSP better satisfied the Langmuir model. The Langmuir fitting model, which mainly describes monolayer sorption, is therefore more accurate in describing the sorption process of GO onto BSP. This indicates that the positively-charged BSP mainly adsorbs GO on active sorption sites through electrostatic interactions (see Fig. 16 and 17).

3.3.1. Analysis of sorption thermodynamic parameters

It is clear that ln$K$ and $1/T$ are linearly correlated, observing Fig. 18. The formulae describing these quantities in more detail are as follows (Xu et al., 2022):

$$K = K_d^p Q_m^{-m} C_b^q \tag{9}$$

$$K^q = K(C^o)^{n-p}(Q^q)^{m-p} \tag{10}$$

$$\ln K^\theta = \frac{\Delta s^\theta}{R} - \frac{\Delta H^\theta}{RT} \tag{11}$$

$$\triangle G = \triangle H - T \times \triangle S \tag{12}$$

$$\triangle G = -RT \ln K^\theta \tag{13}$$

Here, R is the ideal gas constant, generally 8.3145 J/(mol·K), ΔG is the Gibbs free energy (kJ/mol), ΔH is the enthalpy change (kJ/mol), ΔS

is the entropy change (kJ/(mol·K), and T is the absolute temperature (K) (see Fig. 17).

The mechanism of the effect of temperature on the sorption process can be further explained using thermodynamic parameters, as shown in Table 6. As the GO concentration increases, the change in enthalpy gradually decreases, indicating that the disorder of the whole system gradually decreases. The change in Gibbs free energy (ΔG) was negative from the beginning to the end, meaning that the sorption of GO by the BSP was a spontaneous process. For the same concentrations, an increase in temperature increases the absolute value of ΔG, indicating that a rise in temperature within the experimental temperature range can improve sorption capacity (Deng et al., 2021), which is aligned with the isotherm fitting results mentioned earlier. The positive values of ΔH at different C_0 indicate that the sorption of BSP on GO is a heat-absorbing reaction. The isotherm fitting results are consistent with this analysis. The positive value of ΔS increases the randomness of adsorbent molecules and enhances the liquid–solid interface in the sorption phenomenon (Chowdhury and Balasubramanian, 2014), and the enthalpy and entropy changes are both greater than zero, which suggests that the sorption process can occur autonomously at high temperatures (Abdelmonem et al., 2024).

3.4. Desorption study

The desorption efficiency of BSP/GO as measured using the chemical stripping method is shown in Fig. 19. The desorption rate gradually increases as the pH increases from 2 to 10. This result indicates that the interaction force between GO and BSP is stronger under acidic conditions, while the interaction force between BSP and GO weakens as the alkalinity of the environment increases. This is consistent with the adsorption results described earlier. From the graph, it can be seen that after 3 desorption cycles, the desorption rate of BSP/GO at a pH of 10 is 86 %. Therefore, desorption in a strong alkaline environment is suitable for BSP/GO. BSP is from a type of igneous rock rich in iron, magnesium, and calcium. Its mineral composition mainly consists of plagioclase, pyroxene, and olivine. Under alkaline conditions, the surfaces of these minerals are more prone to react with alkaline components in the solution (Allam et al., 2022), forming new mineral phases or altering the surface characteristics of the minerals; accordingly, the surface roughness increases and the desorption capacity is enhanced. In addition, the pH value of the solution affects the electrostatic charge properties of the solid surface. As the pH value increases, the negative charge on the mineral surface increases, which facilitates the adsorption of positively-

P. Jiang et al.

Arabian Journal of Chemistry 17 (2024) 105805

Table 7
Comparison of research results.

Adsorbents	Adsorbate	pH	Adsorbent quality (mg)	Adsorbate concentration(mg/L)	Adsorption capacity(mg/g)	Optimal removal rate (%)	Reference
Iron tailings	GO	7	50	60	51.55	–	(Zhou et al., 2021)
Red Sandstone	GO	4	40	80	89.08	89.08	(Li et al., 2022)
vesicular basalt rock	chromium (III)	6	–	–	–	54.67	(Alemu et al., 2019)
FA-χ	Cd (II)	–	–	–	141.1	–	(Abdallah and Taha, 2012)
SiO2/CS	Uranium (VI)	3.5	60	200	165	–	(Vareda, 2023)
MgO-AC	Cadmium (II)	7	20	25	649.9	95 %	(Haghseresht and Lu, 1998)
Cel/PAN/AO	cadmium (II)	5	–	50	123.23	–	(Deng et al., 2021)
BSP	GO	3	70	80	112	99	

charged substances. Under alkaline conditions, the BSP surface may carry a more negative charge, thus exhibiting stronger repulsion towards GO. Overall, BSP is a material that can effectively adsorb GO, having the potential to reduce environmental pollution and provide a cleaner and healthier living environment. This could contribute to the prevention and reduction of GO toxicity-related diseases, as well as the preservation of ecosystems.

3.5. The adsorption mechanism

A series of experiments have demonstrated the excellent adsorption capacity of BSP for GO. Therefore, understanding the adsorption mechanism is crucial for designs that enhance the interaction between the adsorbent and the adsorbate. According to Table 7, electrostatic forces, hydrogen bonding, and π-π interactions are considered the three main factors influencing the adsorption efficiency. The GO surface carries a high negative charge, making it suitable for adsorption through electrostatic forces. Experimental results have shown that the effective adsorption of GO by BSP is attributed to the presence of calcium cations in the mineral composition of the BSP, which allow for the building of electrostatic forces and the adsorption of GO salt from negatively-charged aqueous solutions, typically due to carboxyl groups. Therefore, the presence of cations enhances the adsorption capacity of BSP. Additionally, the weakening of characteristic peaks of hydroxyl groups in the FT-IR spectrum of GO suggests the formation of hydrogen bonding between GO and BSP, further facilitating the adsorption of GO. The desorption test results of BSP/GO indicate that BSP as an adsorbent has a high desorption rate in an alkaline environment (with a pH of 10), showing promise for practical engineering applications.

4. Conclusion

The experimental results showed that pH, adsorbent mass, and initial concentration had strong effects on the sorption effect of BSP on GO. The best sorption result was achieved at a pH of 3, a BSP mass of 70 mg, and a GO concentration of 80 mg/L, with the sorption removal rate reaching 99 %. Furthermore, SEM and TEM images showed that GO can effectively adhere to the surface of BSP, FTIR results showed that the characteristic peaks of the main constituent materials of BSP were found in the BSP/GO material, and XRD results further verified the cross-linking sorption of GO by BSP. The results of adsorption thermodynamic experiments indicated that within the experimental temperature range, an increase in temperature is beneficial for the adsorption of GO by BSP. The Langmuir fitting model was the most effective in describing and predicting the sorption process of GO onto BSP, and the sorption of BSP on GO was found to be a spontaneous, heat-absorbing chemical reaction. The fitting results of kinetic equations showed that the sorption process of BSP onto GO was best described by quasi-primary kinetics, that the reaction between BSP and GO did not involve complex intermediates,

and that the reaction occurred rapidly within 500 min, reaching sorption equilibrium after 1440 min (24 h). Finally, the desorption experiment showed that the desorption rate of BSP after three washes in an alkaline environment (with a pH of 10) reached 86 %, indicating that BSP has promising prospects for engineering applications and waste remediation.

CRediT authorship contribution statement

Ping Jiang: Writing – review & editing. **Fuping Wang:** Writing – review & editing. **Wei Wang:** Writing – review & editing. **Na Li:** Writing – review & editing. **Shimeng Yu:** Writing – review & editing.

Declaration of competing interest

The authors declare the following financial interests/personal relationships which may be considered as potential competing interests: Wei Wang reports financial support was provided by the National Natural Science Foundation of China. If there are other authors, they declare that they have no known competing financial interests or personal relationships that could have appeared to influence the work reported in this paper.

Acknowledgement

References

Abdallah, R., Taha, S., 2012. Biosorption of methylene blue from aqueous solution by nonviable Aspergillus fumigatus. Chem. Eng. J. 195, 69–76. https://doi.org/10.1016/j.cej.2012.04.066.

Abdelmonem, H.A., Hassanein, T.h.F., Sharafeldin, H.E., Gomaa, H., Ahmed, A.S.A., Abdel-lateef, A.M., Allam, E.M., Cheira, M.F., Eissa, M.E., Tilp, A.H., 2024. Cellulose-embedded polyacrylonitrile/amidoxime for the removal of cadmium (II) from wastewater: Adsorption performance and proposed mechanism. Colloids Surf. A Physicochem. Eng. Asp. 684, 133081 https://doi.org/10.1016/j.colsurfa.2023.133081.

Al-Bermany, E., Chen, B., 2021. Preparation and characterisation of poly (ethylene glycol)-adsorbed graphene oxide nanosheets. Polym. Int. 70 (3), 341–351. https://doi.org/10.1002/pi.6140.

Alemu, A., Lemma, B., Gabbiye, N., 2019. Adsorption of chromium (III) from aqueous solution using vesicular basalt rock. Cogent Environ. Sci. 5 (1), 1650416. https://doi.org/10.1080/23311843.2019.1650416.

Allam, Eman M., Taysser A. Lashen, Saeyda A. Abou El-Enein, Mohamed A. Hassanin, Ahmed K. Sakr, Mohamed Y. Hanfi, M. I. Sayyed, Jamelah S. Al-Otaibi, and Mohamed F. Cheira. 2022, Cetylpyridinium bromide/polyvinyl chloride for substantially efficient capture of rare earth elements from chloride solution. Polymers, , 14(5): 954. DOi: 10.3390/polym14050954.

Allam, E.M., Lashen, T.A., Abou, S.A., El-Enein, M.A., Hassanin, A.K., Sakr, M.F., Cheira, A.A., Hanfi, M.Y., Sayyed, M.I., 2022. Rare earth group separation after extraction using sodium diethyldithiocarbamate/polyvinyl chloride from lamprophyre dykes leachate. Materials 15 (3), 1211. https://doi.org/10.3390/ma15031211.

Almeida, L.N.B., Josue, T.G., Nogueira, O.H.L., Ribas, L.S., Fuziki, M.E.K., Tusset, A.M., Santos, O.A.A., Lenzi, G.G., 2022. The adsorptive and photocatalytic performance of granite and basalt waste in the discoloration of basic dye. Catalysts 12 (10), 1076. https://doi.org/10.3390/catal12101076.

An, B.-H., Da-Mao, Xu., Geng, R., Cheng, Y., Qian, R.-B., Tang, X.-C., Fan, Z.-Q., Chen, H.-B., 2023. The pretreatment effects of various target pollutant in real coal gasification gray water by coupling pulse electrocoagulation with chemical precipitation methods. Chemosphere 311, 136898. https://doi.org/10.1016/j.chemosphere.2022.136898.

Ando, N., Matsui, Y., Kurotobi, R., Nakano, Y., Matsushita, T., Ohno, K., 2010. Comparison of natural organic matter sorption capacities of super-powdered activated carbon and powdered activated carbon. Water Res. 44 (14), 4127–4136. https://doi.org/10.1016/j.watres.2010.05.029.

Anuma, S., Mishra, P., Bhat, B.R., 2021. Polypyrrole functionalized Cobalt oxide Graphene (COPYGO) nanocomposite for the efficient removal of dyes and heavy metal pollutants from aqueous effluents. J. Hazard. Mater. 416, 125929 https://doi.org/10.1016/j.jhazmat.2021.125929.

Bandara, P., Peña-Bahamonde, J., Rodrigues, D., 2020. Redox mechanisms of conversion of Cr (VI) to Cr (III) by GO-polymer composite. Sci. Rep. 10, 1–8. https://doi.org/10.1038/s41598-020-65534-8.

Bytešníková, Z., Koláčková, M., Dobešová, M., Švec, P., Ridošková, A., Pekárková, J., Přibyl, J., Cápal, P., Húska, D., Adam, V., Richtera, L., 2023. New insight into the biocompatibility/toxicity of GOs and their reduced forms on Chlamydomonas reinhardtii. NanoImpact 31, 100468. https://doi.org/10.1016/j.impact.2023.100468.

Cai, D., Song, M., 2007. Preparation of fully exfoliated graphite oxide nanoplatelets in organic solvents. J. Mater. Chem. 17, 3678–3680. https://doi.org/10.1039/b705906j.

Cheira, M.F., 2020. Solvent extraction of uranium and vanadium from carbonate leach solutions of ferruginous siltstone using cetylpyridinium carbonate in kerosene. Chem. Pap. 74 (7), 2247–2266. https://doi.org/10.1007/s11696-020-01073-w.

Chen, P., Liang, H.W., Lv, X.H., Zhu, H.Z., Yao, H.B., Yu, S.H., 2011. Carbonaceous nanofiber membrane functionalized by beta-cyclodextrins for molecular filtration. ACS Nano 5 (7), 5928–5935. https://doi.org/10.1021/nn201719g.

Chen, X., Xia, L., Huang, Y., Lv, Y., Kong, M., Li, Y., 2021. Flow-mediated interaction between graphene oxide nanosheets and polycarbonate chains. J. Phys. Chem. C 125 (7), 4146–4154. https://doi.org/10.1021/acs.jpcc.0c09218.

Chowdhury, S., Balasubramanian, R., 2014. Recent advances in the use of graphene-family nanoadsorbents for removal of toxic pollutants from wastewater. Adv. Colloid Interface Sci. 204, 35–56. https://doi.org/10.1016/j.cis.2013.12.005.

Chupakhin, O. N., Varaksin, M. V., Utepova, I. A., & Rusinov, V. L. 2009 SN H Reactions of ferrocenyllithium and azine N-oxides. DOi: 10.3998/ark.5550190.0010.622.

Deng, Z., Lu, G., Fu, L., Wang, W., Zheng, B., 2021. Investigation of the behavior and mechanism of action of ether-based polycarboxylate superplasticizers sorption on large bibulous stone powder. Materials 14, 2736. https://doi.org/10.3390/ma14112736.

Eissa, M.E., Sakr, A.K., Hanfi, M.Y., Sayyed, M.I., Al-Otaibi, J.S., Abdel-lateef, A.M., Cheira, M.F., Abdelmonem, H.A., 2023. Physicochemical investigation of mercury sorption on mesoporous thioacetamide/chitosan from wastewater. Chemosphere 341, 140062. https://doi.org/10.1016/j.chemosphere.2023.140062.

Fan, H.-T., Zhao, C.-Y., Liu, S., Shen, H., 2017. Sorption characteristics of chlorophenols from aqueous solution onto graphene. J. Chem. Eng. Data 62, 1099–1105. https://doi.org/10.1021/acs.jced.6b00918.

Fouad, M., 2023. Physical characteristics and Freundlich model of sorption and desorption isotherm for fipronil in six types of Egyptian soil. Curr. Chem. Lett. 12, 207–216. https://doi.org/10.5267/j.ccl.2022.8.003.

Gomaa, H., Shenashen, M.A., Elbaz, A., Kawada, S., El-Nasr, T.A., Cheira, M.F., Eid, A.I., El-Safty, S.A., 2021. Inorganic-organic mesoporous hybrid segregators for selective and sensitive extraction of precious elements from urban mining. J. Colloid Interface Sci. 604, 61–79. https://doi.org/10.1016/j.jcis.2021.07.002.

Haghseresht, F., Lu, G., 1998. Sorption characteristics of phenolic compounds onto coal-reject-derived adsorbents. Energy Fuel 12, 1100–1107. https://doi.org/10.1021/ef9801165.

Hassanin, M.A., Negm, S.H., Youssef, M.A., Sakr, A.K., Mira, H.I., Mohammaden, T.F., Al-Otaibi, J.S., Hanfi, M.Y., Sayyed, M.I., Cheira, M.F., 2022. Sustainable Remedy Waste to Generate SiO2 Functionalized on Graphene Oxide for Removal of U(VI) Ions. Sustainability 14, 2699. https://doi.org/10.3390/su14052699.

Indujalekshmi, J., Krishnan, P., Reji, R., Biju, V., 2023. L-ascorbic acid-reduced graphite oxide as active material for supercapacitors. Mater. Today:. Proc. https://doi.org/10.1016/j.matpr.2023.02.159.

Jiang, P., Zhou, L., Wang, W., Li, N., Zhang, F., 2022. Performance and mechanisms of fly ash for GO removal from aqueous solution. Environ. Sci. Pollut. Res. 29, 3773–3783. https://doi.org/10.7763/ijesd.2012.v3.251.

Kalsoom, A., Batool, R., 2020. Biological and nonbiological approaches for treatment of Cr (VI) in Tannery Effluent. Emerg. Eco-Friendly Green Technol. Wastewater Treatment 147–170. https://doi.org/10.1007/978-981-15-1390-9_7.

Kumar, G., Masram, D.T., 2021. Sustainable synthesis of MOF-5@ GO nanocomposites for efficient removal of rhodamine B from water. ACS Omega 6, 9587–9599. https://doi.org/10.1021/acsomega.1c00143.

Li, N., Dai, W., Kang, H., Lv, B., Jiang, P., Wang, W., 2022. Study on the sorption performance and sorption mechanism of GO by red sandstone in aqueous solution. Sorption Sci. Technol. https://doi.org/10.1155/2022/2557107.

Li, N., Fang, J., Jiang, P., Li, C., Kang, H., Wang, W., 2022. Sorption properties and mechanism of attapulgite to GO in aqueous solution. Int. J. Environ. Res. Public Health 19 (5), 2793. https://doi.org/10.3390/ijerph19052793.

Li, N., Dai, W., Kang, H., Lv, B., Jiang, P., Wang, W., 2022. Study on the adsorption performance and adsorption mechanism of graphene oxide by red sandstone in aqueous solution. Adsorpt. Sci. Technol. https://doi.org/10.1155/2022/2557107.

Lim, S., Kim, J.H., Park, H., Kwak, C., Yang, J., Kim, J., Ryu, S.Y., Lee, J., 2021. Role of electrostatic interactions in the sorption of dye molecules by Ti 3 C 2-MXenes. RSC Adv. 11 (11), 6201–6211. https://doi.org/10.1039/d0ra10876f.

Lin, J., Liu, Y., Hu, S., Zhang, Y., Qian, C., Li, A., Zhang, S., 2021. Ultra-fast sorption of four typical pollutants using magnetically separable ethanolamine-functionalized graphene. Sep. Purif. Technol. 271, 118862 https://doi.org/10.1016/j.seppur.2021.118862.

Liu, J., Zhang, J., Xing, L., Wang, D., Wang, L., Xiao, H., Ke, J., 2021. Magnetic Fe3O4/attapulgite hybrids for Cd (II) adsorption: performance, mechanism and recovery. J. Hazard. Mater. 412, 125237 https://doi.org/10.1016/j.jhazmat.2021.125237.

Marcano, D.C., Kosynkin, D.V., Berlin, J.M., Sinitskii, A., Sun, Z., Slesarev, A., Aleant, L. B., Lu, W., Tour, J.M., 2010. Improved synthesis of GO. ACS Nano 4 (8), 4806–4814. https://doi.org/10.1021/nn1006368.

Matsuka, T., Suzuki, M., Matsushita, H., Yokota, H., Sakai, K., 2022. Properties of concrete using crushed stone powder with various specific surface areas. Acta Polytechnica CTU Proceedings 33, 363–369. https://doi.org/10.14311/APP.2022.33.0363.

Mollaamin, F., Monajjemi, M., 2023. Molecular modelling framework of metal-organic clusters for conserving surfaces: Langmuir sorption through the TD-DFT/ONIOM approach. Mol. Simul. 49, 365–376. https://doi.org/10.1080/08927022.2022.2159996.

Pak, H., Phiri, J., We, J., Jung, K., Oh, S., 2021. Adsorptive Removal of Arsenic and Lead by Stone Powder/Chitosan/Maghemite Composite Beads. Int. J. Environ. Res. Public Health 18, 8808. https://doi.org/10.3390/ijerph18168808.

Rout, D.R., Jena, H.M., 2021. Removal of malachite green dye from aqueous solution using reduced GO as an adsorbent. Mater. Today:. Proc. 47, 1173–1182. https://doi.org/10.1016/j.matpr.2021.03.406.

Rout, D.R., Jena, H.M., 2021. Synthesis of novel reduced GO decorated β-cyclodextrin epichlorohydrin composite and its application for Cr (VI) removal: Batch and fixed-bed studies. Sep. Purif. Technol. 278, 119630 https://doi.org/10.1016/j.seppur.2021.119630.

Rout, D.R., Jena, H.M., 2022. Synthesis of novel epichlorohydrin cross-linked β-cyclodextrin functionalized with reduced GO composite adsorbent for treatment of phenolic wastewater. Environ. Sci. Pollut. Res 29, 73444–73460. https://doi.org/10.1007/s11356-022-21018-y.

Rout, D.R., Jena, H.M., 2023. Synthesis of GO-modified porous chitosan cross-linked polyaniline composite for static and dynamic removal of Cr (VI). Environ. Sci. Pollut. Res. 30, 22992–23011. https://doi.org/10.2139/ssrn.4139173.

Sakr, A.K., Abdel Aal, M.M., Abd El-Rahem, K.A., Allam, E.M., Abdel Dayem, S.M., Elshehy, E.A., Hanfi, M.Y., Alqahtani, M.S., Cheira, M.F., 2022. Characteristic aspects of uranium (VI) adsorption utilizing nano-silica/chitosan from wastewater solution. Nanomaterials 12 (21), 3866. https://doi.org/10.3390/nano12213866.

Samuel, O., Othman, M.H.D., Kamaludin, R., Dzinun, H., Imtiaz, A., Li, T., El-badawy, T., Khan, A.U., Puteh, M.H., Yuliwati, E., Kurniawan, T.A., 2023. Photocatalytic degradation of recalcitrant aromatic hydrocarbon compounds in oilfield-produced water: A critical review. J. Clean. Prod. 137567 https://doi.org/10.1016/j.jclepro.2023.137567.

Seabra, A.B., Paula, A.J., de Lima, R., Alves, O.L., Durán, N., 2014. Nanotoxicity of graphene and graphene oxide. Chem. Res. Toxicol. 27 (2), 159–168. https://doi.org/10.1021/tx400385x.

Semghouni, H., Bey, S., Figoli, A., Criscuoli, A., Benamor, M., Drioli, E., 2020. Chromium (VI) removal by Aliquat-336 in a novel multiframe flat sheet membrane contactor. Chem. Eng. Process.-Process Intensific. 147, 107765 https://doi.org/10.1016/j.cep.2019.107765.

Shen, W., Wu, J., Du, X., Li, Z., Wu, D., Sun, J., Wang, Z., Huo, X., Zhao, D., 2022. Cleaner production of high-quality manufactured sand and ecological utilization of recycled stone powder in concrete. J. Clean. Product. 375, 134146 https://doi.org/10.1016/j.jclepro.2022.134146.

Sysoev, V.I., Yamaletdinov, R.D., Plyusnin, P.E., Okotrub, A.V., Bulusheva, L.G., 2023. Sorption kinetics of NO 2 gas on oxyfluorinated graphene film. PCCP 25 (3), 2084–2089. https://doi.org/10.1039/d2cp04926k.

Vareda, J.P., 2023. On validity, physical meaning, mechanism insights and regression of sorption kinetic models. J. Mol. Liq. 121416 https://doi.org/10.1016/j.molliq.2023.121416.

Xiang, L.i., Niu, C.-G., Tang, N., Lv, X.-X., Guo, H., Li, Z.-W., Liu, H.-Y., Lin, L.-S., Yang, Y.-Y., Liang, C., 2021. Polypyrrole coated molybdenum disulfide composites as adsorbent for enhanced removal of Cr (VI) in aqueous solutions by sorption combined with reduction. Chem. Eng. J. 408, 127281 https://doi.org/10.1016/j.cej.2020.127281.

Xu, C., Wang, X., Zhu, J., 2008. Graphene− metal particle nanocomposites. J. Phys. Chem. C 112, 19841–19845. https://doi.org/10.1021/jp807989b.

Xu, Y., Xia, H., Zhang, Q., Jiang, G., Cai, W., Hu, W., 2022. Adsorption of cadmium (II) in wastewater by magnesium oxide modified biochar. Arab. J. Chem. 15 (9), 104059 https://doi.org/10.1016/j.arabjc.2022.104059.

Yaroshenko, Y. G., Lipunov, Y. I., Smakhanov, A. B., & Stolyarova, M. V. 2018, Application of Water-Air Cooling Technologies for Heat Treatment of Bearing Rings. DOi: 10.17073/0368-0797-2018-6-423-430.

Zhang, B., Li, Y., Wu, T., Sun, D., Chen, W., Zhou, X., 2018. Magnetic iron oxide/GO nanocomposites: Formation and interaction mechanism for efficient removal of methylene blue and p-tert-butylphenol from aqueous solution. Mater. Chem. Phys. 205, 240–252. https://doi.org/10.1016/j.matchemphys.2017.11.015.

Zhang, X.J., Wang, G.S., Cao, W.Q., Wei, Y.Z., Liang, J.F., Guo, L., Cao, M.S., 2014. Enhanced microwave absorption property of reduced GO (RGO)-MnFe2O4

nanocomposites and polyvinylidene fluoride. ACS Appl. Mater. Interfaces 6 (10), 7471–7478. https://doi.org/10.1021/am500862g.

Zhang, Y., Wu, L., Deng, H., Qiao, N., Zhang, D., Lin, H., Chen, Y., 2021. Modified GO composite aerogels for enhanced sorption behavior to heavy metal ions. J. Environ. Chem. Eng. 9 (5), 106008 https://doi.org/10.1016/j.jece.2021.106008.

Zhao, R., Li, Y., Ji, J., Wang, Q., Li, G., Wu, T., Zhang, B., 2021. Efficient removal of phenol and p-nitrophenol using nitrogen-doped reduced GO. Colloids Surf. A Physicochem. Eng. Asp. 611, 125866 https://doi.org/10.1016/j.colsurfa.2020.125866.

Zhao, J., Liu, L., Li, F., 2015. GO: Phys. Appl. Vol. 1.

Zhao, S., Wang, Y., Duo, L., 2021. Biochemical toxicity, lysosomal membrane stability and DNA damage induced by GO in earthworms. Environ. Pollut. 269, 116225 https://doi.org/10.1016/j.envpol.2020.116225.

Zhou, J., Yao, L., Wang, Y., Zhao, W., Gu, J., 2021. Study on the adsorption properties of iron tailings for GO. Coatings 11 (7), 768. https://doi.org/10.3390/coatings11070768.